

PAPER

[View Article Online](#)
[View Journal](#) | [View Issue](#)Cite this: *Nanoscale*, 2023, **15**, 1609

Rare-earth-doped indium oxide nanosphere-based gas sensor for highly sensitive formaldehyde detection at a low temperature†

Xiangyun Ma,^a Houjuan Zhu,^b Long Yu,^a Xin Li,^a Enyi Ye,^{b,c} Zibiao Li,^{b,c} Xian Jun Loh^b and Suhua Wang^{*a}

Formaldehyde (HCHO) is widely viewed as a carcinogenic volatile organic compound in indoor air pollution that can seriously threaten human health and life. Thus, there is a critical need to develop gas sensors with improved sensing performance, including outstanding selectivity, low operating temperature, high responsiveness, and short recovery time, for HCHO detection. Currently, doping is considered an effective strategy to raise the sensing performance of gas sensors. Herein, various rare earth elements-doped indium oxide (RE-In₂O₃) nanospheres were fabricated as gas sensors for improved HCHO detection via a facile and environmentally solvothermal method. Such RE-In₂O₃ nanosphere-based sensors exhibited remarkable gas-sensing performance, including a high selectivity and stability in air. Compared with pure, Yb-, Dy-doped In₂O₃ and different La ratios doped into In₂O₃, 6% La-doped In₂O₃ (La-In₂O₃) nanosphere-based sensors demonstrated a high response value of 210 to 100 ppm at 170 °C, which was around 16 times higher than that of the pure In₂O₃ sensor, and also exhibited a detection limit of 10.9 ppb, and a response time of 30 s to 100 ppm HCHO with a recovery time of 160 s. Finally, such superior sensing performance of the 6% La-In₂O₃ sensors was proposed to be attributed to the synergistic effect of the large specific surface area and enhanced surface oxygen vacancies on the surface of In₂O₃ nanospheres, which produced chemisorbed oxygen species to release electrons and provided abundant reaction sites for HCHO gas. This study sheds new light on designing nanomaterials to build gas sensors for HCHO detection.

Received 9th September 2022

Accepted 11th December 2022

DOI: 10.1039/d2nr04972d

rsc.li/nanoscale

1 Introduction

Formaldehyde (HCHO) is a colorless, flammable, pungent odorous volatile organic compound.¹ With the continuous development of industry, HCHO is widely used in textiles, furniture, and other daily necessities thanks to its excellent adhesion.² However, a narrow indoor environment is very unfavorable for the diffusion and oxidative decomposition of HCHO, which makes HCHO one of the most important components of indoor pollutants. HCHO has a pungent odor, so it can also be smelled at low concentrations. Usually people's

olfactory threshold for HCHO is 0.06–0.07 mg m⁻³. IARC specifically classifies HCHO as a class I carcinogen, and as a causative factor for nasopharyngeal carcinoma and leukemia.³ It has been found that long-term exposure to HCHO can lead to headache, dizziness, and sensory disturbance. In addition, HCHO can also cause respiratory dysfunction and liver poisoning. In severe cases, it can lead to gene mutations.⁴ Due to the toxicity of HCHO, the World Health Organization (WHO) has set the exposure limit of HCHO to 0.07 ppm within 30 min.³ OSHA has also set an allowable exposure limit of 0.75 ppm HCHO for an 8 h workday.⁵ Therefore, from the perspective of health and environmental protection, monitoring the concentration of HCHO in the environment is of great significance.

In recent decades, with the rapid development of the Internet of Things (IoT), many gas sensors have been developed to detect toxic and harmful gases. Sensors can give more accurate information than human senses. In particular, gas sensors based on a metal oxide semiconductor (MOS) have received extensive attention. Compared with traditional detection methods, it has the characteristics of miniaturization, low cost, easiness to manufacture, and portability.⁶ Therefore, it

^aGuangdong Provincial Key Laboratory of Petrochemical Pollution Process and Control, School of Environmental Science and Engineering, Guangdong University of Petrochemical Technology, Maoming, Guangdong 525000, China

^bInstitute of Materials Research and Engineering, A*STAR (Agency for Science, Technology and Research), Singapore 138634

^cInstitute of Sustainability for Chemicals, Energy and Environment (ISCE2) A*STAR (Agency for Science, Technology and Research), Singapore 138634

† Electronic supplementary information (ESI) available. See DOI: <https://doi.org/10.1039/d2nr04972d>

has important applications in monitoring human health and detecting toxic gases. At present, many metal oxide semiconductors have been reported to be used to detect HCHO, such as ZnO,⁷ SnO₂,⁸ NiO,⁹ and TiO₂.¹⁰ Among them, indium oxide (In₂O₃), as an n-type semiconductor with an appropriate band gap, has become a kind of sensor material with great development potential by virtue of its superior electronic and optical properties.^{11,12} Gu *et al.* reported the synthesis of In₂O₃ nanoparticles with excellent HCHO gas-sensing performance, whose response to 100 ppm HCHO could reach 80 at 150 °C.¹³ This showed that In₂O₃-based nanomaterials have great application potential in the field of HCHO detection. However, pure In₂O₃ still has the problems of a low response, high operating temperature, and poor selectivity, which limit its practical application.¹⁴ In this regard, researchers have adopted many methods to improve the sensing performance of pure In₂O₃, such as by constructing two-dimensional (2D) and three-dimensional (3D) nanomaterials, forming nanocomposites, doping metal impurities, and through light excitation.^{15,16} It has been reported that the rare earth (RE) element doping of In₂O₃ can change the microstructure of a material, thereby effectively improving the gas-sensing properties of a material.¹⁷ Thangaraj *et al.* found that doping Tb³⁺ could effectively improve the response of In₂O₃ nanoparticles to ethanol.¹⁸ Wang *et al.* found that the response value of Nd-doped In₂O₃ porous nanotubes to 100 ppm of HCHO was 48, which was significantly higher than that of pure In₂O₃.¹⁹ Therefore, the doping of rare earth elements can greatly improve the gas-sensing performance of In₂O₃-based sensors, which gives us some inspiration for the detection of HCHO and to question whether the modification of In₂O₃-based sensors with rare earth elements can show better performance in the detection of HCHO. Therefore, rare earth (RE) element modification can greatly improve the gas-sensing performance of In₂O₃-based sensors, and at the same time has great poten-

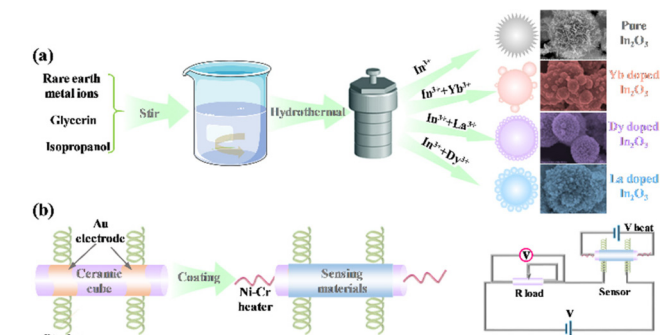


Fig. 1 Schematic diagram of the preparation of different RE-In₂O₃ nanospheres (a) and their use in the design of a gas sensor (b).

tial in the detection of HCHO. However, to the best of our knowledge, there are relatively few studies on HCHO sensors based on RE-doped In₂O₃ (RE-In₂O₃).

In this work, we prepared various RE-element-doped In₂O₃ (RE-In₂O₃) nanospheres by a simple and environmentally friendly solvothermal method (Fig. 1a) and studied the doping effect of different REs and doped lanthanum (La) ratios on the gas-sensing performances of In₂O₃ sensors for HCHO detection (Fig. 1b). Through comparing the structure, gas response, and detection limit, RE-In₂O₃ nanospheres were found to effectively improve the sensing performance of In₂O₃, with lanthanum-doped In₂O₃ (La-In₂O₃) nanospheres exhibiting the optimized performance with high response values of 210 to 100 ppm at 170 °C, a detection limit of 10.9 ppb, and outstanding selectivity and stability. Further compared with doping 3% and 9% La into In₂O₃, the 6% La-In₂O₃-based sensor possessed the best gas-sensing properties. These results were attributed to the fact that the incorporation of RE elements into nanospheres can enlarge the specific surface area and enhance surface oxygen vacancies on the surface of the In₂O₃ nanospheres.²⁰ Therefore, RE-In₂O₃ could be expected to be a strong candidate for the detection of HCHO in practice.



Houjuan Zhu

Houjuan Zhu received her PhD degree in Chemistry from the University of Science and Technology of China in 2015, and then she respectively worked as a Research Fellow at Nanyang Technological University (NTU) from 2015 to 2017 and at National University of Singapore (NUS) from 2018–2021. Currently, she is working at the Institute of Materials Research and Engineering (IMRE), A-STAR.

Her research focuses on the design and synthesis of various nanomaterials, including two-dimensional nanosheets, transition metal dichalcogenides quantum dots, and semiconducting polymer nanoparticles, in bioimaging, cancer therapy, antibacterial, biosensing, and photocatalysis.

2 Experimental

All the chemical reagents in the experiments were of analytical grade and used as received without further purification.

2.1 Preparation of pure and RE-doped In₂O₃ nanospheres

A typical synthesis was as follows: In (NO₃)₃·xH₂O (0.5 g) and 6 mol% (LaCl₃·6H₂O, DyCl₃·6H₂O, YbCl₃·6H₂O) solution were respectively dispersed in 48 mL of isopropanol and stirred for 30 min. Subsequently, 16 g of glycerin was added to the aforementioned solution and stirred for 1 h. The above solution was then transferred to an autoclave and heated at 180 °C for 6 h, and then the autoclave was cooled to room temperature. The reacted mixture was centrifuged at 8000 rpm and washed 3–5 times with distilled water and absolute ethanol to obtain a solid product, followed by drying at 80 °C for 12 h. The pro-

ducts were heated from room temperature to 350 °C at a rate of 5 °C min⁻¹ under an air atmosphere to produce RE-In₂O₃.

2.2 Characterization of RE-In₂O₃ nanospheres

The powder X-ray diffraction patterns were obtained using a Rigaku Ultima IV system (Cu K α , λ = 1.54051 Å) in the range of 5°–80° at room temperature. The morphological and elemental composition were observed by field emission scanning electron microscopy (FE-SEM, JEOL) along with elemental mapping. Nitrogen (N₂) adsorption–desorption isotherms were collected at 77 K on an ASAP 2460 instrument (Micromeritics). The surface areas were determined by the Brunauer–Emmett–Teller (BET) method. The element compositions were characterized by X-ray photoelectron spectroscopy (XPS) on a Thermo Escalab 250 electron spectrometer using Al K irradiation.

2.3 Fabrication of a gas sensor device based on RE-In₂O₃ nanospheres

The preparation process of the RE-In₂O₃ sensor device was as follows. First, the synthetic sample was mixed with a certain amount of deionized water in an agate mortar to form a uniform slurry, and then was coated with ceramics. The film was formed by drying at natural temperature. A Ni–Cr heating wire was inserted into the ceramic tube as a heater, and the working temperature was controlled by controlling the heating current. It was then welded to a black hexagonal base. Finally, it was put on an AS-20 sensor aging stage and aged for 10 h under 115 mA heating current. A schematic diagram of the RE-In₂O₃ sensor is shown in Fig. 1b. The Ni–Cr heating wire was inserted into the ceramic tube as the heater, and the optimal operating temperature was controlled by controlling the heating current.

2.4 Gas-sensing measurements

The working principle and sensing performance of the sensor were tested with the gas-sensing analysis system. In the gas-sensing experiment, when the relative humidity of the air was about 50% (in Maoming City, Guangdong Province, the relative humidity is usually high), the air was used as the background gas. Liquid volume calculation software (Elite. Tech.) was used to calculate the volume of liquid with the required concentration injected into the gas chamber, and then the right amount of liquid was injected into the evaporating dish set in the gas chamber with a microsyringe, and then evaporated completely at a temperature higher than its boiling point. The response of the sensor is defined as $S = R_a/R_g$, where R_a represents the resistance of the sensor in the air atmosphere, and R_g represents the resistance of the sensor in the target gas.

3 Results and discussion

3.1 Structural and morphological characterization

RE-In₂O₃ nanospheres and pure In₂O₃ were fabricated using a mixture of RE ions and glycerine as a precursor solution by a simple one-step solvothermal method, as presented in Fig. 1a.

The morphologies and microstructures of the as-synthesized RE-In₂O₃ nanospheres and pure In₂O₃ were studied by scanning electron microscopy (SEM). As shown in Fig. 2a, pure In₂O₃ showed irregular nanoflowers with good monodispersity and uniformity formed by the self-assembly of nanosheets composed of small nanospheres. With the doping of RE elements, the morphology of RE-In₂O₃ changed into a relatively uniform large nanosphere assembled from small nanospheres, as depicted in Fig. 2(b–d). It was evident that no other morphologies could be found from the panoramic SEM images, showing a high yield of these nanostructures. From the enlarged SEM images in Fig. 2(b–d), different-sized small nanospheres were observed to grow on the surface of a big nanosphere. These adjacent nanospheres were in contact with each other, enabling the gas to migrate to the internal space of the material, thereby increasing the response of the material to HCHO vapor. Also, the sizes of the small nanospheres were found to decline with the doped rare earth elements changing from Yb, to La, to Dy, making RE-In₂O₃ materials with different improved gas-sensing performances for HCHO detection.

To preliminarily understand the chemical elemental distribution in these nanostructures, elemental mapping was further performed of the RE-In₂O₃ nanospheres and pure In₂O₃ and the results are shown in Fig. 3. As expected, In (green) and O (cyan) elements could be clearly detected in the selected area of both the pure In₂O₃ nanoflowers and RE-In₂O₃ nanospheres, showing the successful formation of In₂O₃ nanostructures. Besides this, Yb (red), Dy (violet), and La (blue) elements could also be observed and were homogeneously distributed and showed no apparent element separation or aggregation in Yb-In₂O₃ (Fig. 3h), Dy-In₂O₃ (Fig. 3l), or La-In₂O₃ (Fig. 3p), respectively. These findings indicated that the RE (La, Yb, and Dy) dopants were effectively bound to the surface of the In₂O₃ sensing materials. Furthermore, to further show the chemical composition of the pure In₂O₃ and RE-In₂O₃

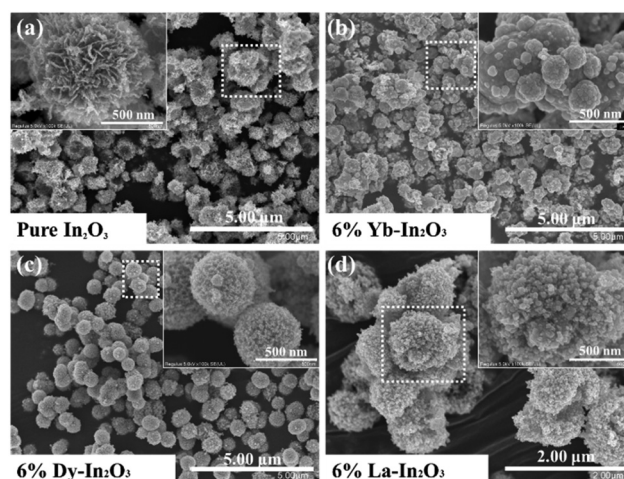


Fig. 2 SEM images of pure-In₂O₃ nanoflowers (a), Yb-In₂O₃ nanospheres (b), Dy-In₂O₃ nanospheres (c), and La-In₂O₃ nanospheres (d).

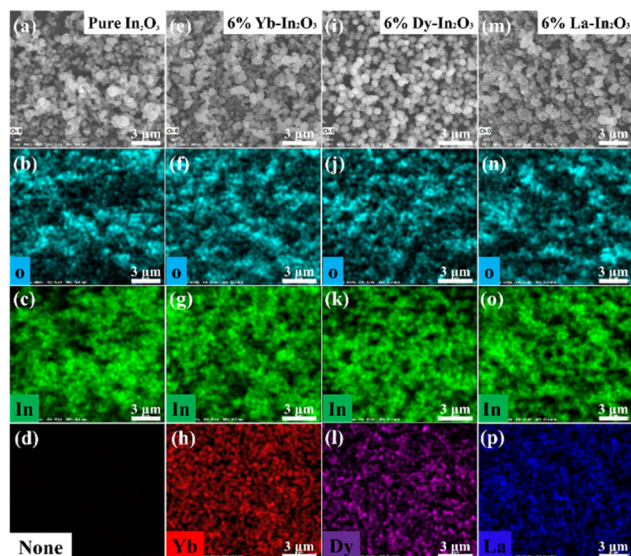


Fig. 3 FESEM images and elemental mapping images of pure In_2O_3 nanoflowers (a–d), $\text{Yb-In}_2\text{O}_3$ nanospheres (e–h), $\text{Dy-In}_2\text{O}_3$ nanospheres (i–l), and $\text{La-In}_2\text{O}_3$ nanospheres (m–p), scale bar: 3 μm .

nanospheres, the corresponding electron dispersive spectroscopy (EDS) was used to analyze their element amounts (Fig. S1†). Obviously, the EDS spectra showed that there were oxygen (O) and indium (In) in both the pure In_2O_3 and RE- In_2O_3 nanospheres, as well as the presence of Yb, Dy, and La in the corresponding RE-doped In_2O_3 nanostructures, which was consistent with the results from the element mapping. In addition, the ratios of the doped RE elements and In element in the 6% $\text{La-In}_2\text{O}_3$, 6% $\text{Yb-In}_2\text{O}_3$, and 6% $\text{Dy-In}_2\text{O}_3$ were respectively about 6.04%, 6.26%, and 6.06%, showing that there were no additional pollutants in the synthesized samples.

To explore the crystalline structure of these In_2O_3 nanostructures, the X-ray diffraction (XRD) spectra for all the samples were determined. From Fig. 4a, it could be clearly observed that the XRD peaks for pure In_2O_3 and RE- In_2O_3 were a little wide and strong, suggesting their relatively good crystallinity. It was notable that the major diffraction peaks of all the samples were located at around 21.50° , 30.58° , 37.69° , 39.81° , 40.80° , 45.69° , 51.02° , and 60.67° , corresponding to the (211),

(222), (411), (420), (422), (431), (440), and (622) lattice planes, respectively, which were in good agreement with the peaks of cubic-phase In_2O_3 (JCPDS Card No. 71-2194). In addition, the RE- In_2O_3 nanospheres did not show obvious impurity peaks, indicating that the doping of RE elements did not generate the RE oxide crystal phase, or significantly damage the cubic structure of In_2O_3 .

At the same time, according to the calculation by the Scherrer formula in eqn (1),²¹ where λ is the X-ray wavelength (1.54056 Å), and θ and β are respectively the Bragg diffraction angle and the peak width at half maximum. With the doping of RE elements, the average grain sizes of $\text{Dy-In}_2\text{O}_3$, $\text{La-In}_2\text{O}_3$, and $\text{Yb-In}_2\text{O}_3$ were calculated to be respectively 15.06, 15.46, and 22.14 nm, which were higher than that of pure In_2O_3 (8.23 nm), as shown in Table 1, indicating the incorporation of RE ions could effectively prevent the grain growth of In_2O_3 . Furthermore, the ion radii of Yb^{3+} , Dy^{3+} , and La^{3+} were respectively 0.868, 0.912, and 1.032 Å, which were all larger than that of In^{3+} (0.81 Å). With the introduction of these RE ions into the In_2O_3 lattice, the lattice positions of In^{3+} were replaced to induce an increase in the interplanar spacing (d) of In_2O_3 lattice.²² In detail, the variations in RE- In_2O_3 were investigated through calculating the lattice constant and microstrain (ϵ) (Table 1), which were determined by eqn (2) and (3).

$$D = \frac{0.89 \times \lambda}{\beta \times \cos \theta} \quad (1)$$

$$d_{hkl} = \frac{a}{\sqrt{h^2 + l^2 + k^2}} \quad (2)$$

$$2\epsilon = \Delta d / 2d \quad (3)$$

It can be observed from Table 1 that the lattice constant was increased to a certain extent when doping in RE ions, which may be attributed to higher radius of the doping ions and aliovalent substitution. Apart from this, the microstrain (ϵ) was also found to be gradually increase. This could be due to the lattice contraction resulting from the lattice constant, finally causing structural defects in the RE- In_2O_3 nanospheres.

In addition, the interaction between the doping ratios of the RE elements with the In_2O_3 lattice was investigated by XRD. As depicted in Fig. 4b, no change was observed in the

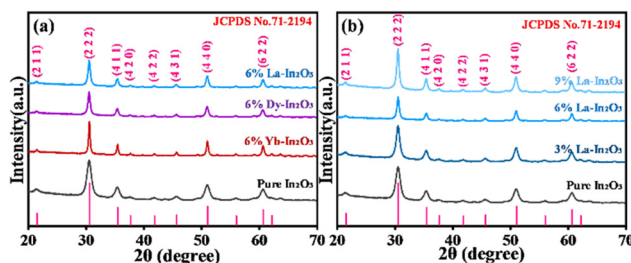


Fig. 4 XRD patterns of (a) pure In_2O_3 and 6% RE- In_2O_3 and (b) 0%, 3%, 6%, and 9% $\text{La-In}_2\text{O}_3$.

Table 1 Grain sizes, lattice constants, and microstrains of all the samples

Samples	Grain size, D (nm)	λ (Å)	Lattice constant, $a = b = c$ (Å)	d_{222} (Å)	Microstrain, ϵ (%)
Pure In_2O_3	8.23	1.54056	10.1348	2.925664	
6% $\text{Yb-In}_2\text{O}_3$	22.14	1.54056	10.13545	2.925852	0.003197605
6% $\text{Dy-In}_2\text{O}_3$	15.06	1.54056	10.14128	2.927537	0.031976739
3% $\text{La-In}_2\text{O}_3$	10.34	1.54056	10.14178	2.927681	0.034439011
6% $\text{La-In}_2\text{O}_3$	15.46	1.54056	10.14188	2.927707	0.034886698
9% $\text{La-In}_2\text{O}_3$	13.07	1.54056	10.14328	2.928113	0.041809892

diffraction peaks with increasing the La doping ratios when comparing the major peaks of the four samples, thus showing no influence of the La doping ratio on the crystal In_2O_3 lattice. Also, from Table 1, the average grain sizes of $\text{La-In}_2\text{O}_3$ all increased, which effectively inhibited the grain growth of In_2O_3 with the incorporation of 3%, 6%, and 9% of La^{3+} , being a maximum at 6% doping, which may be one reason behind this structure having the best gas-sensing performance. Furthermore, with the doping ratios of La^{3+} increasing from 0 to 9%, the interplanar spacing, lattice constants, and micro-strain all increased. Such phenomena could be explained from the greater introduction of La^{3+} , which led to more aliovalent substitution of In^{3+} by La^{3+} with a larger radius, also inducing more lattice distortion and contraction in the In_2O_3 lattice, and thus generating more structural defects in $\text{La-In}_2\text{O}_3$.

To further study the internal architectures, N_2 adsorption-desorption isotherm curves for the pure In_2O_3 and $\text{RE-In}_2\text{O}_3$ nanospheres were applied. As shown in Fig. S2,[†] the isotherms for the four samples presented with type V shapes, which clearly showed that all the In_2O_3 samples had mesoporous features according to the IUPAC classification. Moreover, the specific surface areas of the pure In_2O_3 , $\text{Yb-In}_2\text{O}_3$, $\text{Dy-In}_2\text{O}_3$, and $\text{La-In}_2\text{O}_3$ nanospheres tested by BET were 37.71, 68.80, 52.13, and 70.77 $\text{m}^2 \text{g}^{-1}$, respectively. The large specific surface area of such composites is an important factor for an adsorbed target gas because of the ability to support abundant reaction sites for facilitating gas molecular diffusion, consequently inducing improved gas-sensing performance.

To identify the chemical composition and valence states of the oxygen species of the pure In_2O_3 and $\text{RE-In}_2\text{O}_3$ NPs, X-ray photoelectron spectroscopy (XPS) was employed. All the binding energies were charge corrected with reference to the 284.5 eV for the C 1s line.²³ In particular, as shown in the magnified corresponding O 1s spectra of the pure In_2O_3 and $\text{RE-In}_2\text{O}_3$ in Fig. 5a, the chemical state of oxygen and the relative concentration of different oxygen states were analyzed by high-resolution XPS. It was obvious that the O 1s XPS spectra of the four samples were deconvoluted into two separate peaks by the best fitting, where the peak at a lower binding energy of 529.5 ± 0.3 eV was attributed to the crystal lattice oxygen (O_L) and the one at the position of 531.1 ± 0.2 eV (O_V) was ascribed to oxygen adsorbed on the surface of In_2O_3 .^{24,25} The corresponding area ratios of each component peak represented the contents of the two oxygen species in these samples, as shown in Fig. 5b. Clearly, the doping of RE elements was observed to significantly change the surface concentration of these oxygen species on the surface. It was acknowledged that the chemisorbed oxygen (O_V) acted as an electron donor and played a significant role in the detection of gas. The proportion of O_V in the $\text{RE-In}_2\text{O}_3$ nanospheres from the doping of Yb to La gradually increased from 51.72% to 72.81%, and they were all higher than that of the pure In_2O_3 nanoflowers, indicating that the doping of RE elements into the In_2O_3 lattice facilitated the increased adsorbed oxygen, thus improving the gas-sensing performance. This phenomenon may be related to the improved moisture resistance of metal oxides by doping metal

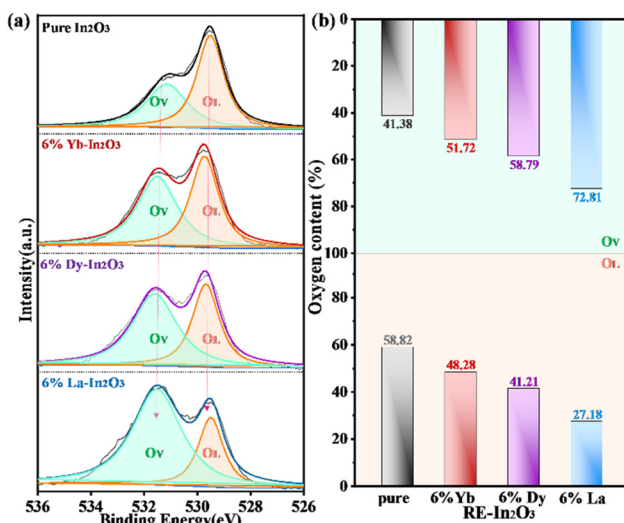


Fig. 5 O 1s high-resolution XPS spectra of the pure In_2O_3 , $\text{RE-In}_2\text{O}_3$ nanospheres, O_V : chemisorbed oxygen; O_L : crystal lattice oxygen. (b) Relative contents of O_V and O_L in oxygen species of the pure In_2O_3 , $\text{RE-In}_2\text{O}_3$ nanospheres.

elements^{26,27} and the abundant reaction sites supported by the nanosphere structure with a large specific surface area. Specially, among these $\text{RE-In}_2\text{O}_3$ nanospheres, $\text{La-In}_2\text{O}_3$ significantly increased the highest content of O_V accompanied with the highest content of lattice oxygen (O_L) being reduced, which may also be the main reason for the $\text{La-In}_2\text{O}_3$ sensor having the best sensing performance for HCHO.²⁸

3.2 Gas-sensing properties of $\text{RE-In}_2\text{O}_3$

The optimum working temperature is an important factor for a material's surface state during measuring the gas-sensing performance. To determine the optimal operating temperature of the nanoparticle sensor based on pure In_2O_3 and $\text{RE-In}_2\text{O}_3$, we investigated the response of the four sensors to 100 ppm of HCHO to obtain the optimum working temperature (Fig. 6a). As displayed in Fig. 6b, the four sensors showed similar behaviors at different temperatures from 120 °C to 300 °C, where the response values of the four sensors increased with the increase in the working temperature until reaching the maximum value. This may be ascribed to the fact that it was hard for the adsorbed HCHO molecules to get enough thermal energy to react with the oxygen species at lower working temperature, following which the molecular motion could accelerate with the working temperature increasing. Thus, we could clearly see in Fig. 6b that the response values of the pure In_2O_3 and $\text{Yb-In}_2\text{O}_3$ sensors reached the maximum at 220 °C, while the maximum was at 170 °C for $\text{La-In}_2\text{O}_3$ and $\text{Dy-In}_2\text{O}_3$. However, as the temperature increased further, the response value started to decrease, which was mainly because the desorption rate of HCHO was higher than the adsorption rate, and thus there was a large ratio of HCHO gas overflow.^{16,29} Compared with the pure In_2O_3 and other $\text{RE-In}_2\text{O}_3$, the response value of $\text{La-In}_2\text{O}_3$ to 100 ppm HCHO at 170 °C

reached the best maximum at about 210, indicating the promotion effect of doping RE elements.

The dynamic response/recovery curves of the pure In_2O_3 and RE- In_2O_3 sensors with the concentration of HCHO increasing from 1 to 300 ppm are shown in Fig. 6c. It could be seen that the response of both the pure In_2O_3 and RE- In_2O_3 sensors gradually increased with the increase in HCHO concentration, and the response enhancement to HCHO increased from the pure In_2O_3 sensor to the La- In_2O_3 sensor. Correspondingly, the curve of the responses in the concentration range of HCHO for these sensors at 170 °C was also investigated, as shown in Fig. 6d. These sensors displayed a stepwise distribution as the HCHO concentration increased from 1 to 300 ppm, and there was a good linear relationship for the four sensors for their sensor response and HCHO concentration from 1 to 100 ppm and from 100 to 300 ppm. Obviously, among these sensors, the slopes of the straight lines for the 6% La- In_2O_3 gas-sensing material were the largest in the two concentration ranges, implying that the 6% La- In_2O_3 sensor exhibited the highest sensitivity and the best gas-sensing properties. The selectivity is another critical prerequisite for gas sensors. Thus, the selectivity of the pure In_2O_3 and RE- In_2O_3 sensors for a variety of gases, including ethanol, HCHO, isopropanol, acetone, and methanol, at 170 °C was further investigated. From Fig. 6e, it could be clearly seen that all the sensors had a higher response to HCHO gas over other gases, and RE- In_2O_3 possessed a higher response to HCHO compared with the pure In_2O_3 . By contrast, the response value of La- In_2O_3 to HCHO gas over various gases was the highest, showing the excellent selectivity of RE- In_2O_3 toward HCHO at

the optimum working temperature. This result may indicate that the energy that was needed when various gas molecules reacted with adsorbed oxygen during the surface reaction process of the sensing materials may have existed at the appropriate resource levels. However, when this energy could not be obtained enough at lower temperature or of the gas got away from the surface of the sensing materials under the higher temperature, the preferred gas response could not be reached. Apparently, HCHO gas herein was more easily adsorbed and reacted on the surface of the RE- In_2O_3 sensors, especially the La- In_2O_3 sensors. Furthermore, continuous gas response measurements were also performed on the pure In_2O_3 and RE- In_2O_3 sensors to study the long-term stability of the sensor, as shown in Fig. 6f. Obviously, the response values for the four sensors did not change even within 30 days, suggesting the outstanding long-term stability of the In_2O_3 -based sensors, paving the foundation for HCHO sensing.

3.3 Gas-sensing performance of La- In_2O_3

According to above-mentioned results, the La- In_2O_3 sensor exhibited the best gas-sensing performance for HCHO gas compared with the other RE- In_2O_3 sensors, such as the lowest operating temperature, and the highest sensitivity and selectivity. Therefore, we further studied the gas-sensing performance of the La- In_2O_3 sensor in detail (Fig. 7a). The response of the four La- In_2O_3 sensors with doping 0%, 3%, 6%, 9% La to 100 ppm HCHO at different operating temperatures were studied, as shown in Fig. 7b. As can be seen, the optimum operating temperature of La- In_2O_3 was 170 °C, and the response value of the 6% La- In_2O_3 sensor (about 210) was the

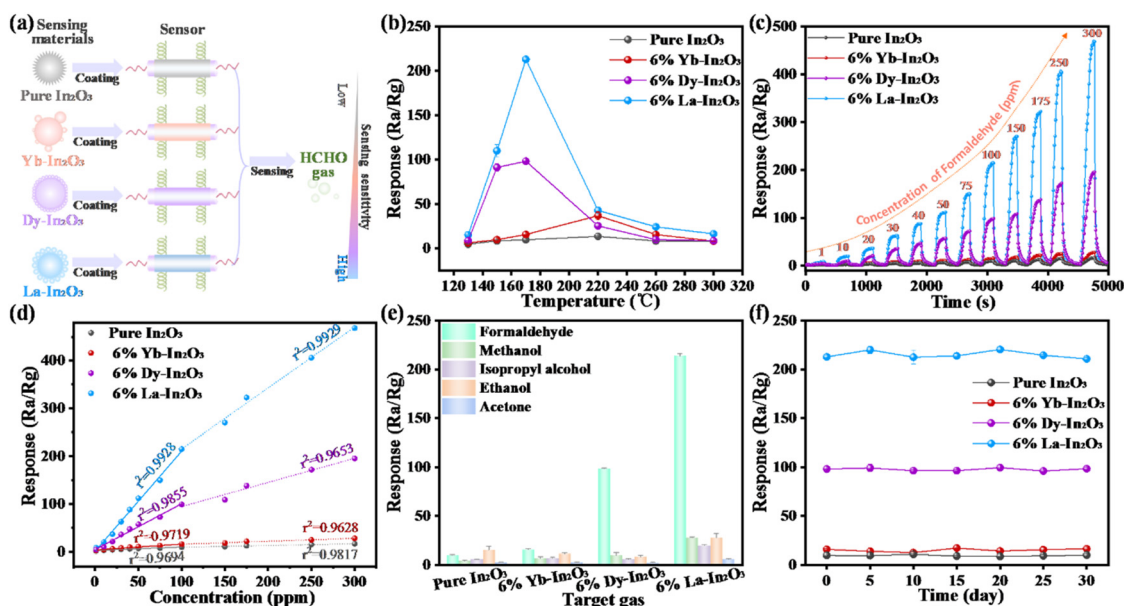


Fig. 6 (a) Diagram for sensing HCHO by the RE- In_2O_3 nanosphere-based gas sensor. (b) Response of the four sensors based on pure In_2O_3 and RE- In_2O_3 to 100 ppm HCHO at different operating temperatures. (c) Response of the four sensors based on pure In_2O_3 and RE- In_2O_3 to HCHO with different concentrations (1–300 ppm) at an operating temperature of 170 °C. (d) Response curves of these gas sensors towards different HCHO concentrations. (e) Response of the four sensors based on pure In_2O_3 and RE- In_2O_3 to 100 ppm of different gases. (f) Response versus time curves for assessing the stability of the sensors upon exposure to 100 ppm HCHO.

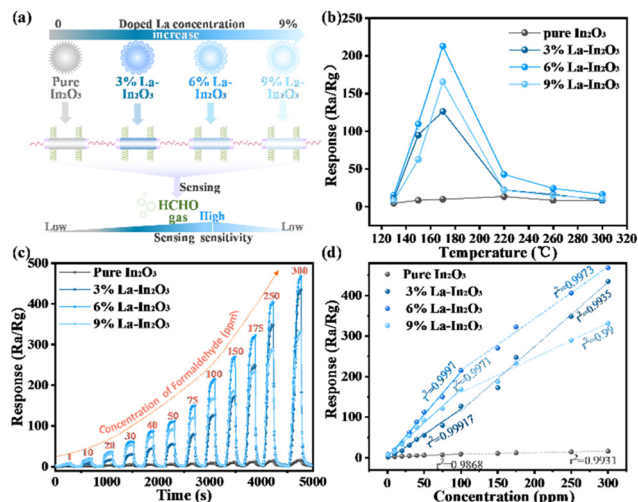


Fig. 7 (a) Schematic illustration showing La-In₂O₃ doped with different levels for HCHO sensing. (b) Response of the four sensors based on *x* La-In₂O₃ (*x* = 0%, 3%, 6%, 9%) to 100 ppm HCHO at different operating temperatures. (c) Typical responses of the two sensors based on *x* La-In₂O₃ (*x* = 0%, 3%, 6%, 9%) La-In₂O₃ in the HCHO concentration range of 1–300 ppm at 170 °C. (d) Linear relationship between the response and HCHO concentration from 1 to 300 ppm.

highest, which was nearly 1.68, 1.29, and 16 times that of the 3%, 9% La-In₂O₃ sensor and pure In₂O₃ sensor (about 13), respectively. Therefore, 6% was considered as the best doping ratio of La-In₂O₃. To display the dynamic response curves of the four 0%, 3%, 6%, 9% La-In₂O₃-based sensors to 100 ppm HCHO, the relationship between their response values and the concentration of HCHO were investigated. Fig. 7c displays that the response values of the four sensors increased with the HCHO concentration increasing in the range from 1 to 300 ppm and that the 6% La-In₂O₃ sensors exhibited the best response enhancement. At the same time, the response linearity is an important criterion for the success of sensors. A good response linearity could give the sensor the ability to perform quantitative detection. From Fig. 7d, a linear relationship between the HCHO concentration and the response of the four La-In₂O₃ sensors at 170 °C could be observed. It was not difficult to find that a good linearity of these sensors could be obtained in the HCHO concentration ranges of 1–100 ppm and 100–300 ppm respectively. The slopes and the *R*² values are shown in Table S1,[†] indicating the high correlation and good linear relationship. Also, the theoretical detection limit (TDL) of the gas sensors could be calculated by the following formula (eqn (4)).³⁰

$$\text{TDL} = \frac{3 \text{ rms}_{\text{noise}}}{\text{slope}} \quad (4)$$

where *rms*_{noise} and slope respectively represent the root mean square error of the baseline and the slope value of the linear curve. So, it could be calculated that the TDLs of the 3%, 6% and 9% La-In₂O₃ sensors were respectively 18.7, 10.9, and 14.0 ppb, which were all lower than that of the Yb-In₂O₃ sensor

(183 ppb) and Dy-In₂O₃ (24.0 ppb) sensor. The result showed that the 6% La-In₂O₃ sensors possessed the lowest TDL, and the TDLs for the La-In₂O₃ and Dy-In₂O₃ sensors both met the international standard for the indoor detection of the HCHO concentration (70 ppb).³¹

In the actual working environment, there are often multiple gases at the same time, so the selectivity of the sensor to HCHO gas is very important. To demonstrate the selectivity of the La-In₂O₃ sensors, the cross-selectivity of the four sensors under the same conditions to several typical gases, including ethanol, HCHO, acetone, isopropanol, and methanol were tested (Fig. 8a). Apparently, it could be seen that the sensors based on the 3%, 6%, and 9% La-In₂O₃ samples showed a higher response to HCHO than the other gases compared to pure In₂O₃. Noted that there was no obvious response for both the La-In₂O₃ and pure In₂O₃ sensors to these contrasted gases. These results indicated the excellent selectivity of the La-In₂O₃ sensors to HCHO gas, laying the foundation for future HCHO testing in practice. Additionally, good stability is conducive to the long-term use of the sensor in practical work. The stability of the sensor based on La-In₂O₃ nanospheres was tested every five days for one month, as shown in Fig. 8b. It can be seen from the figure that the response of the four sensors to 100 ppm HCHO at 170 °C still kept constant without significant drift even within 30 days, proving the outstanding long-time stability of the four sensors. Simultaneously, the influence of humidity on the response of the La-In₂O₃ sensors was also studied (Fig. S3[†]). There were no obvious effects on the response of the sensor to HCHO under a relative humidity of 30%–60%. However, it was found that when the relative humidity increased further from 70% to 90% RH, the response began to sharply drop from about 189 to 10. Note that when the humidity was close to 100%, the sensor had almost no

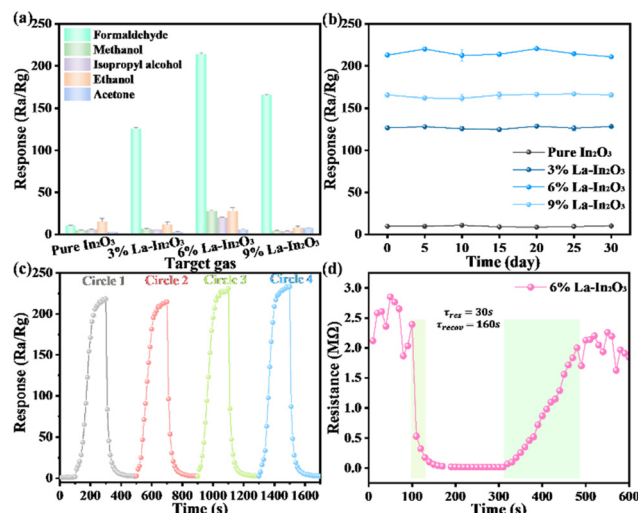


Fig. 8 (a) Response of *x* La-In₂O₃ (*x* = 0%, 3%, 6%, 9%) to 100 ppm of different gases. (b) Response time curves for the stability of the four sensors upon exposure to 100 ppm HCHO. (c) Cyclic response curve of the sensor and (d) the dynamic response–recovery curves of the sensor based on 6% La-In₂O₃ nanospheres.

response. Also, the good reproducibility of a sensor plays an important role in gas sensing. Thus, the continuous reproducibility of the sensor based on 6% La-In₂O₃ nanospheres was further investigated. As shown in Fig. 8c, no matter whether exposed to HCHO vapor or air, the response value of this sensor was relatively stable even after four cycles, indicating that the sensor had good reproducibility and reversibility. The dynamic response characteristics of the sensor based on 6% La-In₂O₃ nanospheres at 170 °C were studied. Fig. 8d obviously displays that this sensor had a continuous and intact response–recovery curve with a short response time of 30 s and recovery time of 160 s for 100 ppm HCHO, respectively.

Lastly, some nanomaterials have been designed for HCHO detection so far. So a comparison of the gas-sensing performance of several MOS-based gas sensors for detecting HCHO was performed and the results are briefly summarized in Table 2.^{32–38} In consideration of all the gas-sensing properties, such as optimal working temperature, response value, sensi-

tivity, and selectively, the 6% La-In₂O₃ sensor in our work exhibited a relatively better HCHO detection performance compared with the other MOS-based gas sensors. Note that the superior gas response of the RE-In₂O₃ was closely related to the RE element dopant.

3.4 Gas-sensing mechanism of RE-In₂O₃ nanospheres

In₂O₃ nanomaterials, as an n-type semiconductor with electron carriers, are acknowledged to be a conventional chemiresistor sensing material with an easily noted change of their electrical features derived from the surface reaction of In₂O₃. According to the current gas-sensing theory of In₂O₃, In₂O₃ generally detect a gas *via* changing its resistance value through the surface adsorbed oxygen and reaction between gas molecules and the surface electron. As presented in the HCHO-sensing diagram of Fig. 9a, when pure In₂O₃ nanoflowers were exposed in air at low temperature, the oxygen molecules were absorbed on their surface to produce different chemisorbed oxygen

Table 2 Comparison of the sensing performance of HCHO sensors based on MOS nanostructures

Sensing materials	Structure	HCHO concentration (ppm)	Temperature (°C)	Response (R_a/R_g)	Ref.
6% La-In ₂ O ₃	Nanosphere	100	170	210	This work
In ₂ O ₃	Nanoparticle	100	230	80	13
SnO ₂ /In ₂ O ₃	Hetero-nanofiber	50	375	18.9	32
NiO	Ordered mesoporous nanoparticle	380	300	20.6	33
Ag-loaded In ₂ O ₃	Sunflower-like nanostructure	50	240	20.6	34
Pd-SnO ₂	Hollow nanofiber	100	160	18.8	35
SnO ₂	Mesoporous microtube	100	200	37	36
Pd-SnO ₂	Nanocrystals	100	260	85	37
Ag-LaFeO ₃	Nanofiber	5	230	4.8	38

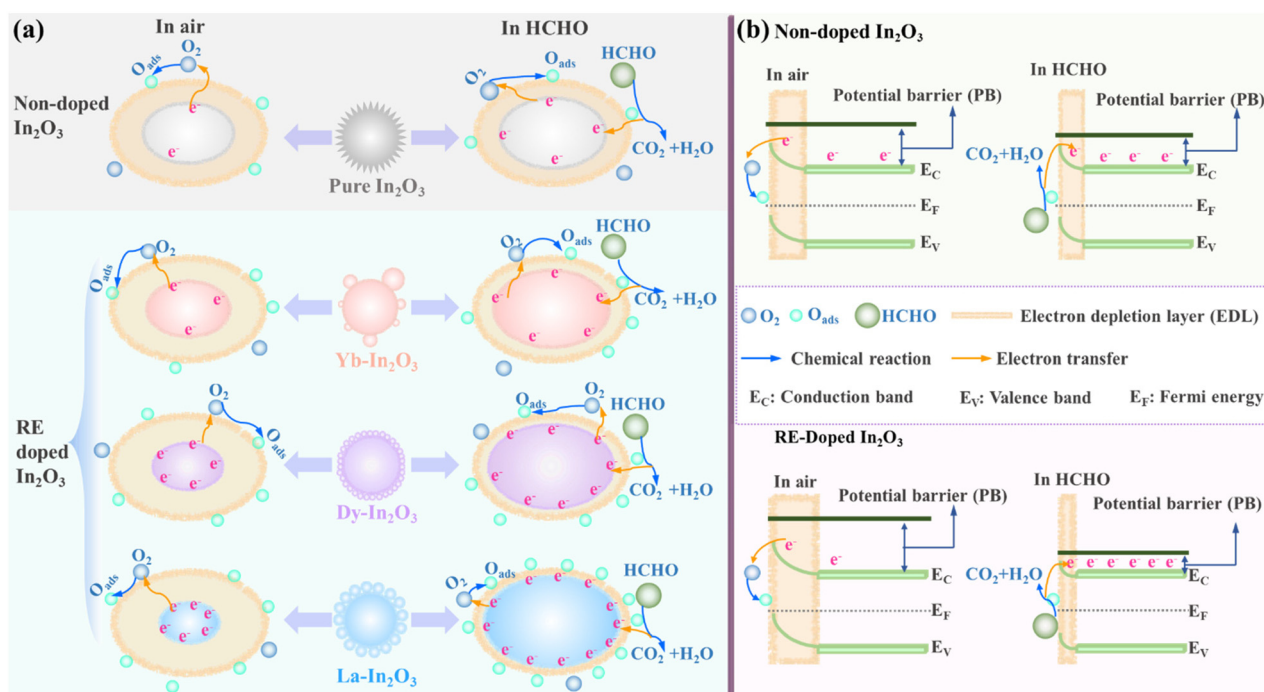
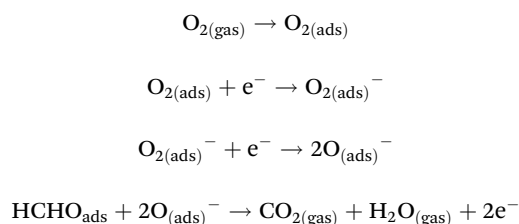


Fig. 9 (a) Schematic mechanism for sensing HCHO by RE-doped In₂O₃ and (b) illustration of their corresponding bands.

species (Q_{ads}), including O^{2-} , O , and O_2^- , via capturing the free electrons (e^-) from the conduction band of In_2O_3 . It should be noted that an electron-depletion layer (EDL) on the surface of In_2O_3 would be formed due to the decreased carrier level and increased resistance. To specially introduce this process in to the electronic structure, the corresponding upward band mechanism is schematically illustrated in Fig. 9b. Notably, a potential barrier (PB) between the air and electrons was also generated in the present situation, except for the EDL. When exposed to HCHO gas, the chemisorbed oxygen species (Q_{ads}) could react with HCHO molecules adsorbed on the sensor surface to release electrons into the conductance band of In_2O_3 , leading to a decline in the EDL thickness, resistance (Fig. 9a) and PB (Fig. 9b). It should be noted that In_2O_3 's resistance value will revert to its initial resistance value within a certain time when In_2O_3 is put back in to air, showing the superior stability and reusability of In_2O_3 as a gas sensor. The possible interaction between O_{ads} and HCHO can be described by the following chemical equations.



With the doping of RE elements into In_2O_3 nanomaterials, the HCHO-sensing performances of RE- In_2O_3 nanospheres were observed to be greatly improved compared to pure In_2O_3 nanoflowers, which could possibly be attributed to the following two aspects, as described in Fig. 9. First, the nanosphere structure enabled the In_2O_3 nanomaterials to have a large specific surface area, leading to abundant reaction sites. Such a change promotes the electron-transfer process and accelerates the surface reaction of the nanospheres, thus inducing a rapid change in the resistance, finally causing an enhanced gas-sensing response. Second, the incorporated RE ions could replace In^{3+} as a donor to realize an enhancement in the surface oxygen vacancies in In_2O_3 , thus having an effective influence on the adsorption behavior. It is well-known that more oxygen vacancies in crystal structures can cause more free electrons, which can be captured and thus can significantly affect the gas-sensing performances. According to XPS analysis, the introduction of RE elements into the crystal structure could lead to abundant adsorbed oxygen, thus promoting surface reactions to finally produce improved gas-sensing features. Additionally, with doping various RE elements from Yb, to Dy, to La into In_2O_3 , the HCHO-sensing properties of La- In_2O_3 were found to be the best, which was mainly may due to the more defect oxygens generated from the more chemisorbed oxygen species (O_{ads}). Based on the same reason, the maximum absorbed oxygen endowed the 6% La- In_2O_3 sensor with the optimum response to the target gas in comparison with the 3% La- In_2O_3 and 9% La- In_2O_3 .

4 Conclusions

In summary, rare earth elements-doped indium oxide (RE- In_2O_3) nanospheres were prepared by respectively doping Yb, Dy, or La ions into In_2O_3 using a facile solvothermal strategy and these were further designed as gas sensors for HCHO detection with improved gas-sensing performance. Such RE- In_2O_3 gas sensors exhibited high stability in air at RT. and selectivity for HCHO in mixtures of five gases, namely ethanol, HCHO, isopropanol, acetone, and methanol. In addition, the 6% La- In_2O_3 based sensor was found to possess the best gas-sensing properties in comparison with that of pure In_2O_3 , Yb- In_2O_3 , Dy- In_2O_3 , as well as La- In_2O_3 with 3% and 9% La. In particular, the 6% La- In_2O_3 nanospheres were demonstrated to not only have a low detection limit of 10.9 ppb, a response time of 30 s to 100 ppm HCHO with a recovery time of 160 s, but also demonstrated a high response value of 210 to 100 ppm at 170 °C, which was around 16 times higher than that of the pure In_2O_3 sensor. Finally, these results were mainly due to the synergistic effect of the large specific surface area and enhanced surface oxygen vacancies on the surface of the In_2O_3 nanospheres, which produced chemisorbed oxygen species to release electrons and provided abundant reaction sites for HCHO gas. This study shows the huge potential of RE- In_2O_3 nanospheres in gas-sensing application toward HCHO.

Author contributions

X. Y. M. and L. Yu performed the sensing investigations and analyzed the data. X. L. verified all the experimental data and draft. H. J. Z. performed the chemical, XRD, electronic XPS studies, analyzed the data and drafted the manuscript with contributions from all authors. Z. B. L., E. Y. Y., X. J. L. and S. H. W. reviewed and edited the manuscript. All authors discussed the experimental results and commented on the manuscript.

Conflicts of interest

There are no conflicts to declare.

Acknowledgements

This work was supported by the National Natural Science Foundation of China (U21A20290, 82001957), the Guangdong Basic and Applied Basic Research Foundation (2022A1515011656).

References

- 1 G. de Falco, M. Barczak, F. Montagnaro and T. J. Badosz, *ACS Appl. Mater. Interfaces*, 2018, **10**, 8066–8076.

- 2 S. El Sayed, L. s. Pascual, M. Licchelli, R. Martínez-Mañez, S. Gil, A. M. Costero and F. Sancenón, *ACS Appl. Mater. Interfaces*, 2016, **8**, 14318–14322.
- 3 K. Kawamura, K. Kerman, M. Fujihara, N. Nagatani, T. Hashiba and E. Tamiya, *Sens. Actuators, B*, 2005, **105**, 495–501.
- 4 H. Zhu, J. She, M. Zhou and X. Fan, *Sens. Actuators, B*, 2019, **283**, 182–187.
- 5 J. Wang, P. Zhang, J.-Q. Qi and P.-J. Yao, *Sens. Actuators, B*, 2009, **136**, 399–404.
- 6 H. Chen, J. Hu, G.-D. Li, Q. Gao, C. Wei and X. Zou, *ACS Appl. Mater. Interfaces*, 2017, **9**, 4692–4700.
- 7 Y. Chen, Y. Zhang, H. Zhang and C. Chen, *Appl. Surf. Sci.*, 2020, **532**, 147446.
- 8 G. Li, Z. Cheng, Q. Xiang, L. Yan, X. Wang and J. Xu, *Sens. Actuators, B*, 2019, **283**, 590–601.
- 9 R. Prajesh, V. Goyal, M. Nahid, V. Saini, A. K. Singh, A. K. Sharma, J. Bhargava and A. Agarwal, *Sens. Actuators, B*, 2020, **318**, 128166.
- 10 S. Zhang, T. Lei, D. Li, G. Zhang and C. Xie, *Sens. Actuators, B*, 2014, **202**, 964–970.
- 11 Q. Qi, P.-P. Wang, J. Zhao, L.-L. Feng, L.-J. Zhou, R.-F. Xuan, Y.-P. Liu and G.-D. Li, *Sens. Actuators, B*, 2014, **194**, 440–446.
- 12 R.-J. Ma, X. Zhao, X. Zou and G.-D. Li, *J. Alloys Compd.*, 2018, **732**, 863–870.
- 13 F. Gu, C. Li, D. Han and Z. Wang, *ACS Appl. Mater. Interfaces*, 2018, **10**, 933–942.
- 14 J.-L. Wang, Q.-G. Zhai, S.-N. Li, Y.-C. Jiang and M.-C. Hu, *Inorg. Chem. Commun.*, 2016, **63**, 48–52.
- 15 D. Han, P. Song, S. Zhang, H. Zhang, Q. Xu and Q. Wang, *Sens. Actuators, B*, 2015, **216**, 488–496.
- 16 Z. Wang, C. Hou, Q. De, F. Gu and D. Han, *ACS Sens.*, 2018, **3**, 468–475.
- 17 Z.-H. Ma, R.-T. Yu and J.-M. Song, *Sens. Actuators, B*, 2020, **305**, 127377.
- 18 K. Anand, J. Kaur, R. C. Singh and R. Thangaraj, *Mater. Sci. Semicond. Process.*, 2015, **39**, 476–483.
- 19 X. Wang, J. Zhang, Y. He, L. Wang, L. Liu, H. Wang, X. Guo and H. Lian, *Chem. Phys. Lett.*, 2016, **658**, 319–323.
- 20 M. Al-Hashem, S. Akbar and P. Morris, *Sens. Actuators, B*, 2019, **301**, 126845.
- 21 P. Praveen, G. Viruthagiri, S. Mugundan and N. Shanmugam, *Spectrochim. Acta, Part A*, 2014, **117**, 622–629.
- 22 J. Bai, Y. Luo, C. Chen, Y. Deng, X. Cheng, B. An, Q. Wang, J. Li, J. Zhou, Y. Wang and E. Xie, *Sens. Actuators, B*, 2020, **324**, 128755.
- 23 F. Li, X. Gao, R. Wang, T. Zhang, G. Lu and N. Barsan, *ACS Appl. Mater. Interfaces*, 2016, **8**, 19799–19806.
- 24 M. Dai, L. Zhao, H. Gao, P. Sun, F. Liu, S. Zhang, K. Shimanoe, N. Yamazoe and G. Lu, *ACS Appl. Mater. Interfaces*, 2017, **9**, 8919–8928.
- 25 L. Gao, F. Ren, Z. Cheng, Y. Zhang, Q. Xiang and J. Xu, *CrystEngComm*, 2015, **17**, 3268–3276.
- 26 M. Anbia and S. E. M. Fard, *J. Rare Earths*, 2012, **30**, 38–42.
- 27 R. Zhang, S. Cao, T. Zhou, T. Fei, R. Wang and T. Zhang, *Sens. Actuators, B*, 2020, **310**, 127695.
- 28 K. Wan, D. Wang, F. Wang, H. Li, J. Xu, X. Wang and J. Yang, *ACS Appl. Mater. Interfaces*, 2019, **11**, 45214–45225.
- 29 Z. Liu, B. Liu, W. Xie, H. Li, R. Zhou, Q. Li and T. Wang, *Sens. Actuators, B*, 2016, **235**, 614–621.
- 30 M. T. Uddin, Y. Nicolas, C. Olivier, T. Toupance, L. Servant, M. M. Müller, H.-J. Kleebe, J. Ziegler and W. Jaegermann, *Inorg. Chem.*, 2012, **51**, 7764–7773.
- 31 H. Long, A. Harley-Trochimczyk, S. Cheng, H. Hu, W. S. Chi, A. Rao, C. Carraro, T. Shi, Z. Tang and R. Maboudian, *ACS Appl. Mater. Interfaces*, 2016, **8**, 31764–31771.
- 32 H. Du, J. Wang, M. Su, P. Yao, Y. Zheng and N. Yu, *Sens. Actuators, B*, 2012, **166–167**, 746–752.
- 33 X. Lai, G. Shen, P. Xue, B. Yan, H. Wang, P. Li, W. Xia and J. Fang, *Nanoscale*, 2015, **7**, 4005–4012.
- 34 S. Wang, B. Xiao, T. Yang, P. Wang, C. Xiao, Z. Li, R. Zhao and M. Zhang, *J. Mater. Chem. A*, 2014, **2**, 6598–6604.
- 35 Y. Lin, W. Wei, Y. Li, F. Li, J. Zhou, D. Sun, Y. Chen and S. Ruan, *J. Alloys Compd.*, 2015, **651**, 690–698.
- 36 W. Zhang, X. Cheng, X. Zhang, Y. Xu, S. Gao, H. Zhao and L. Huo, *Sens. Actuators, B*, 2017, **247**, 664–672.
- 37 G. Li, Y. Fan, Q. Hu, D. Zhang, Z. Ma, Z. Cheng, X. Wang and J. Xu, *J. Alloys Compd.*, 2022, **906**, 163765.
- 38 W. Wei, S. Guo, C. Chen, L. Sun, Y. Chen, W. Guo and S. Ruan, *J. Alloys Compd.*, 2017, **695**, 1122–1127.